Results in Engineering 26 (2025) 104921

Contents lists available at ScienceDirect

Results in Engineering

journal homepage: www.sciencedirect.com/journal/results-in-engineering

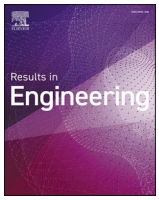

Research paper

# Influence of second metal incorporation on nickel-based unsupported catalysts for $CO_2$ reduction ($CO_2$-SR) Technology

Sofía Essounani-Mérida [a,b], Sergio Molina-Ramírez [a], Marina Cortés-Reyes [a,b], Concepción Herrera [a,b,*], Mª Ángeles Larrubia [a,*], Luis J. Alemany [a,b]

[a] Departamento de Ingeniería Química, Facultad de Ciencias, Universidad de Málaga, Campus de Teatinos, Málaga 29071, Spain
[b] Instituto Universitario de Materiales y Nanotecnología, IMANA, Universidad de Málaga, Campus de Teatinos, Málaga 29071, Spain

ARTICLE INFO

*Keywords:*
$CO_2$-SR technology
$CO_2$ storage
$CH_4$ regeneration
Ni-M bimetallic unsupported catalyst
Ba, Ca, K or Sr

ABSTRACT

The incorporation of alkali or alkaline-earth metals in unsupported Ni-based catalyst was analyzed as a strategy for high-temperature $CO_2$ storage and chemical regeneration via methane, within the framework of $CO_2$ storage–regeneration ($CO_2$-SR) technology. It was observed that the addition of Ba, Ca, Sr and K into the Ni-catalyst modifies not only the textural but also the electronic properties of the catalysts. A restructuring of the unsupported oxide surface occurs by the reduction of the modified Ni-oxide catalyst when exposed to a $H_2$-atmosphere at high temperature (600 °C). Upon oxygen release from NiO lattice, the alkali metals favor the reduction and stabilization of these Ni-metallic species. In such a way, nickel-metallic particles are formed from the NiO-bulk, thus generating unsupported metal catalysts; stabilized by interaction with alkali metals and anchored on the surface. The presence of Ba, Ca, Sr or K in the Ni-based catalyst formulation influences the $CO_2$ storage capacity and regeneration by conversion employing $CH_4$ registering the trend Ca>Ba>*K*>Sr for the catalytic activity at 600 °C in term of $CO_2$ removal capacity and $CH_4$ conversion.

## 1. Introduction

$CO_2$ and $CH_4$ are two significant greenhouse gases, and their concentrations in the atmosphere have been on a consistent rise due to human activities, thereby effectively contributing to climate change. $CO_2$ emissions represent the 81 v/v % of total GHG with the transport and the electricity generation sectors currently making the greatest contribution, with almost 60 % of total emissions, followed by methane with over 12 v/v % [1]. The European Climate Law enshrines the objective set forth in the European Green Deal for Europe's economy and society to become climate-neutral by 2050. Furthermore, the law also establishes the intermediate target of reducing net greenhouse gas emissions by at least 55 % by 2030 in comparison to 1990 levels. After nearly a decade of collaboration and dialogue, the recent United Nations Climate Change Conference, COP29, reached consensus on the key elements that will define the functioning of carbon markets under the Paris Agreement [2]. These commitments are a key factor in advancing Carbon Capture and Utilization (CCU) initiatives and encouraging investment in innovative technologies that not only capture $CO_2$ emissions but also transform them into valuable resources. By including Carbon Capture and Utilization (CCU) in the carbon market framework, COP29 aims to encourage nations and industries to adopt more sustainable alternatives that will help reduce global $CO_2$ emissions [3].

According to the International Energy Agency (IEA), to achieve a sustainable development by 2050, it will be necessary to implement a range of strategies aimed at regulating $CO_2$ emissions and attaining the levels established in the climate summits [4]. These strategies must consider not only the capture of $CO_2$ but also its utilization and transformation into value-added products. To date, these technologies remain in a relatively early stage of development and significant efforts will be required to achieve short-term results with good expectations of future application. The utilization of $CO_2$ and $CH_4$ (GHGs) as carbon sources represents a significant opportunity for the utilization of these gases as a valuable resource. There have been numerous attempts to minimize the emission of $CO_2$ and $CH_4$ to prevent global warming. One of the most promising strategies for the mitigation of anthropogenic $CO_2$ emissions is the conversion of $CO_2$ into chemical fuels and value-added chemicals [5]. The transformation of methane gas into synthesis gas (a mixture of $H_2$ and CO) that can be conveniently processed to produce chemicals and fuels is one of the significant means to address these

* Corresponding authors at: Departamento de Ingeniería Química, Facultad de Ciencias, Universidad de Málaga, Campus de Teatinos, Málaga 29071, Spain.
*E-mail addresses:* concepcionhd@uma.es (C. Herrera), mavargas@uma.es (M.Á. Larrubia).

https://doi.org/10.1016/j.rineng.2025.104921
Received 2 April 2025; Accepted 11 April 2025
Available online 12 April 2025

environmental issues [6,7]. The main utilization routes are catalytic hydrogenation with catalysts derived from metal and metal oxide (chemical reduction of $CO_2$ by hydrogen) for the synthesis of methanol as a transport fuel and the formation of methane for the regulation of the electrical network. The initial approach is oriented towards the production of a commodity and liquid fuel. The second route is the synthesis of methane (methane reaction) that can be produced during off-peak hours and combustion at peak hours to regulate the electricity grid; however, these processes are severely hydrogen-dependent, and it therefore of interest only in the case that the hydrogen comes from a renewable source. $CO_2$ dry reforming with methane (DRM) has attracted significant attention as a process for converting $CO_2$ into syngas (CO and $H_2$), a valuable feedstock for the synthesis of synthetic fuels or higher hydrocarbons through Fischer-Tropsch synthesis [8–12].

In a previous study, Kim et al. [13] demonstrated the feasibility of incorporating a calcium-based $CO_2$ capture process with a subsequent DRM process for the conversion of captured $CO_2$ into syngas. Tian et al. [14] presented the use of a bifunctional sorbent-catalyst (CaO-Ni) for the *in situ* capture of $CO_2$ and its conversion into syngas via DRM. The two pioneering studies offer promising results as a feasible Carbon Capture and Utilization technology (CCU) [15,16]. After the capture stage, the conversion of $CO_2$ into valuable products requires the use of a reducing agent, such as hydrogen or hydrocarbons as $CH_4$, to activate the $C = O$ bond of $CO_2$ molecules for its subsequent conversion [14,17]. Due to the stable molecular structures of $CO_2$ and $CH_4$, dry reforming typically necessitates a high operating temperature above 600 °C and low pressures [18].

The reaction of $CO_2$ with methane (DRM) has attracted significant attention as a means of obtaining synthesis gas (CO and $H_2$). Therefore, the strategy of $CO_2$ revalorization into syngas using $CH_4$, the second most harmful gas in the atmosphere, represents a potential alternative for the simultaneous reduction of two GHG emissions.

Integrated $CO_2$ capture and conversion processes offer the promise of a drastic abatement of $CO_2$ emissions, as well as their valorization into chemical building blocks such as $CH_4$ and CO [19]. This technology takes advantage of the characteristics of the chemical looping process, whereby $CH_4$ and $CO_2$ are fed separately, thus avoiding the limitations imposed by the equilibrium conversion rate in the co-feeding mode [20,21]. The development of advanced materials capable of efficiently capturing $CO_2$ and converting it into valuable chemicals through a one-step reaction with $CH_4$ ("one-pot" process) represents a compelling challenge and an innovative approach. The integration of both capture and conversion in a single reactor and utilizing only a single homogeneous material entails substantial benefits in terms of process intensification. Currently, chemical looping conversions of methane and $CO_2$ have been widely reported [22,23]. It is necessary the presence of an adsorbent component, which is typically composed of alkali metal oxides or alkaline-earth metal oxides such as Ca or Na. Additionally, Li, K and Mg have also been proposed as potential alternatives [19,24,25]. Carbonates, such as the alkali/alkaline-earth carbonates such as $K_2CO_3$ and $BaCO_3$, can be reduced to their respective oxides and hydroxides and act as $CO_2$ capture and storage materials over a wide temperature range, with temperatures expected to be even lower in a reducing atmosphere [26]. The alkali/alkali-earth component provides basic sites for the direct capture of $CO_2$ from flue gas in exhaust systems [27,28]. Thereafter, this can be converted on the same material through the intervention of a metal that must possess the adequate redox properties that allow it to return to its initial condition after being in contact with $CO_2$, in an oxidized atmosphere. Despite the fact that noble metals have been shown to exhibit excellent low-temperature activity in dry reforming processes [29,30], they are not typically preferred due to their high cost [8,31,32].

Ni-based catalysts are a promising type of catalysts that are widely used in DRM reaction. This is due to their low cost and high activity [13,33,34], which improve resistance to coke formation in the DRM [33,35]. The utilization of alkaline earth-Ni has been demonstrated to reduce coke formation [36,37], thereby accelerating the gasification of carbon via reverse Boudouard reaction [37,38]. Ni is capable of activating $CH_4$ and facilitating the migration of lattice oxygen [39], thus playing a crucial role in the activation of reactants [40]. Meanwhile, alkaline or alkaline earth metals are an excellent promising container for oxygen storage.

During the redox process, oxygen vacancies can enhance oxygen transfer and provide an efficient way for the surface reaction to transport oxygen through the bulk network and creates effective surface sites for reagent adsorption and subsequent activation [41].

The $CO_2$ adsorption ability can be attributed to the presence of abundant oxygen vacancies, as evidenced by previous studies [42–44]. The mobility of $O_2$ plays a key role in the efficient capture of $CO_2$ during the initial stage of diffusion-controlled carbonation reaction. The cyclic stability of the $CO_2$ reaction is directly correlated with the presence and abundance of oxygen vacancies in the additives [45]. However, the oxygen vacancy of the catalyst also favors the dissociation of products, thereby improving both the storage capacity and release capacity of oxygen. This results in the lowest $CH_4$ activation and $CO_2$ decomposition temperatures [46]. This provides an efficient way for surface reactions to transport oxygen through the bulk lattice, creating effective surface sites for reactant adsorption and subsequent activation [41]. Additionally, the mitigation of carbon coke deposition may be attributed to the higher concentration of oxygen vacancies [47].

The key to the $CO_2$-SR technology is the use of a redox catalyst, which is required to be capable of activating carbon-species and transferring lattice oxygen. Recently, our Research Group has developed a technology based on the LNT-$NO_x$ technology that operates in alternating stages involving the capture of $CO_2$ (instead of $NO_x$) contained in industrial combustion gases and the chemical revalorization to hydrogen through an internal *in situ* process of reforming with $CH_4$ ($CO_2$-storage-regeneration, $CO_2$-SR technology). The catalytic material must exhibit both capacities at the same time, adsorption and chemical conversion, with the appropriate composition, structure and chemical properties to perform each step of the process [48,49]. The general objective of the research is to develop highly innovative dual function catalytic materials, based in Ni and modified by an alkaline or alkaline-earth metal, to facilitate the production of syn-gas from industrial flue gas emissions, $CO_2$ and $CH_4$, the two most important greenhouse gases.

## 2. Experimental

### 2.1. Catalyst synthesis

A series of four unsupported bimetallic catalysts were synthesized by ultrasonically assisted coprecipitation of a nickel precursor combined with an alkali or an alkaline earth metal (Ba, Ca, K and Sr), using an atomic ratio Ni/Metal =10/1. $Ni(NO_3)_2{\cdot}6H_2O$, $Ba(NO_3)_2$, $Ca(NO_3)_2{\cdot}4H_2O$, $KNO_3$ and $Sr(NO_3)_2$ were used as metal precursors. To the precursor mixture, 3 wt. % LUDOX HS-40 colloidal silica (Aldrich Chemistry, 40 wt. % $SiO_2$ in $H_2O$ and a surface area of 198-258 $m^2{\cdot}g^{-1}$) was added, respect to the total mass of nickel and metal, as nucleating agent and surface promoter. The obtained solution was kept in agitation overnight at 30 °C. Then, 3-times sonications were carried out at room temperature for 15 s using an Ultrasonic Processor UIP1000hd (Hielscher) with a frequency of 20 kHz using a titanium sonotrode and a power intensity of 300 $W{\cdot}cm^{-2}$. Subsequently, ammonia was added dropwise until a pH = 9–10 was reached, depending on the metal used. After co-precipitation, the resulting gel was washed and dried in static air at 90 °C for 12 h, and finally calcined in air at 800 °C (5 °C·$min^{-1}$) for 4 h [48]. These catalysts will henceforth be referred to as NiM, where M represents Ba, K, Ca, or Sr.

### 2.2. Catalysts characterization

The catalysts were characterized by adsorption-desorption of $N_2$ at −196 °C and $CO_2$ at 25 °C on a Micromeritics ASAP 2020 analyzer, in which the solid was previously degassed in vacuum ($10^{-3}$ Pa) at 80 °C. The surface area was determined by the Brunauer-Emmet-Teller (BET) method and pore volume by Barret-Joyner-Halenda (BJH) methods.

X-ray Powder diffraction patterns were collected in the 10–80° (2Θ) range using an X'Pert ProMPD diffractometer (PANanalytical) with *Cu*K$_\alpha$1 radiation (λ = 1.5406 Å) and a Ge (111) primary monochromator. The average crystal size was calculated by *Debye Scherrer* equation.

The X-ray photoelectron spectroscopy technique was carried out using a Physical Electronic spectrometer (model PHI 04–584) employing Al Kα radiation (1486.6 eV, 100 μm, 100 W and 20 kV) as excitation source and a dual-beam charge neutralizer to analyze the elements present in each catalyst. As a reference, the value of the maximum peak of adventitious carbon (C1s), set at a binding energy of 284.8 eV, was used to determine the position of the signals with a deviation of ±0.2 eV. All deconvolutions of experimental curves were done with Gaussian-Lorenzian line fitting of varying proportions (60-80 %).

Raman spectra were recorded on a DXR Raman microscope (ThermoScientific), working at 532 nm and 7 mW and with a Charge Couple Device (CCD) detector. The spectra were collected at room temperature in the Raman shift range 100–2000 $cm^{-1}$ with an accumulation time of 5 s.

Quantitative analysis of the elements Ba, Ca, K, Sr and Ni was performed on an inductively coupled plasma mass spectrometer, ICP-MS Nexion 300D (Perkin Elmer), with a single quadrupole analyzer and a collision cell with He gas. For acid digestion, a Milestone Ultrawave pressure microwave digester was used, using 240 °C temperature and 40 Bar pressure.

Tests to determine $CO_2$ adsorption capacity were performed at atmospheric pressure in a U-shaped fixed bed reactor connected to a Pfeiffer Prisma QMS 200 mass spectrometer. The system was purged in He and then the sample was activated at 600 °C (10 °C·$min^{-1}$) with a stream of 3 % $H_2$ in He for 1 h. After, $CO_2$ adsorption was carried out by feeding at a concentration of 2000 ppm equilibrated in He at the same temperature with a constant total flow rate of 100 mL $min^{-1}$. The value of $CO_2$ stored was calculated by subtraction of the numerical integrated responses for $CO_2$ fed and the $CO_2$ line registered during a rectangular pulse of 2000 ppm of $CO_2$ according to Eq. (1) at 600 °C, for reduced catalyst in $H_2$-atmosphere.

$$\frac{CO_2^{stored}(mol_{CO_2})}{g_{cat}} = \frac{A_{CO_2}^{retained}\cdot F}{g_{cat}} \quad (1)$$

where $A_{CO_2}^{retained}$ is the net adsorbed $CO_2$ and F represents the total fed volumetric gas flow.

$CO_2$-Temperature-Programmed Desorption ($CO_2$-TPD) and Temperature Programmed Reduction ($H_2$-TPR) were determined using a Micromeritics Autochem III instrument. For $CO_2$-TPD, a sample of 15 mg was pretreated with He at 800 °C and a flow rate of 50 ml·$min^{-1}$ for 1 h to remove water and other contaminants. Then, the sample was cooled to room temperature and saturated with 50 ml·$min^{-1}$ of pure $CO_2$ at 60 °C for 10 min. After this, $CO_2$ desorption was performed up to 800 °C with a heating ramp of 30 °C·$min^{-1}$. The $H_2$-TPR were performed in a tubular reactor containing 15 mg of catalyst coupled to a TCD-GC. The sample was reduced in a gaseous mixture of 10 % $H_2$ balanced in Ar from room temperature to 800 °C at 10 °C·$min^{-1}$ with a flow rate of 50 ml·$min^{-1}$.

### 2.3. Catalytic activity in $CO_2$-SR cyclic conditions

To evaluate the catalytic behavior, cyclic $CO_2$ storage and $CH_4$ regeneration steps were performed at a constant temperature of 600 °C and atmospheric pressure using the *Transient Response Method* (TRM). Each gas was introduced in 10-minute pulses with 10,000 ppm of $CO_2$ or $CH_4$ in He, followed by a He purge. The experiments were conducted in a U-shaped fixed-bed reactor connected to a QMS 200 mass spectrometer (Pfeiffer Vacuum Prisma™), using 60 mg of catalyst and a 100 ml·$min^{-1}$ inlet flow to achieve a GHSV of 2.12 × $10^4$ $h^{-1}$. Prior to the experiment, the catalyst was activated *in situ* under a 3 % $H_2$-He atmosphere for 1 h at 600 °C, followed by a He purge until all signals returned to baseline. The selected signals were normalized and calibrated to eliminate any interference between the *m/z* species: 2 ($H_2$), 4 (He), 12 (C), 14 (N), 15 ($CH_4$), 18 ($H_2O$), 28 (CO), 32 ($O_2$), and 44 ($CO_2$). Prior to each experiment, a blank test (without catalyst) was conducted.

The percentage of $CO_2^{stored+converted}$ was calculated according to Eq. (2) and the percentage ( %) of $CH_4$ converted according to Eq. (3).:

$$\%\ CO_2^{removed} = \frac{mol\ CO_2^{stored+converted}}{mol\ CO_2^{in}}\cdot 100 \quad (2)$$

$$\%\ CH_4^{converted} = \frac{mol\ CH_4^{converted}}{mol\ CH_4^{in}}\cdot 100 \quad (3)$$

Where $mol-CO_2^{stored+converted}$=mol-$CO_2^{removed}$ and $mol-CH_4^{converted}$ were obtained by subtraction of the numerical integration of the calibrated MS responses for $CO_2^{in}$ or $CH_4^{in}$ and the $CO_2$ or $CH_4$ line registered during storage and regeneration steps, extended almost for 10 alternating cycles, respectively. Whereas the selectivity values of $H_2$ and CO, as main products in the regeneration step, were calculated from the following equations:

$$S_{H_2} = \frac{mol\ H_2^{produced}}{\sum_{j=0}^{P} mol\ product_j}\cdot 100 \quad (4)$$

$$S_{CO} = \frac{mol\ CO^{produced}}{\sum_{j=0}^{P} mol\ product_j}\cdot 100 \quad (5)$$

## 3. Results and discussion

### 3.1. Catalysts characterization

Structural properties of NiM catalyst are presented in Table 1. As can be seen, all catalysts possessed a higher specific surface area than expected for non-supported material obtained by a similar preparation procedure [50] because of the addition of colloidal silica in the preparation procedure, that act as a promoter of textural properties. They presented a mesoporous structure, with small pore volume (0.07–0.17 $cm^3 \cdot g^{-1}$) and a discrete pore size diameter between 3.6 and 7.5 nm. The incorporation of colloidal silica provides an improvement of textural properties to the catalyst.

Fig. 1a) shows the powder XRD diffraction lines of the NiM catalysts after calcination. The diffraction patterns are sharp and narrow, indicating the presence of a face-centered cubic (FCC) phase, which is consistent with ICDD number 04–016–1090 related to NiO. Characteristic peaks were observed at 37.76°, 43.76°, 63.4°, and 75.6°,

**Table 1**
Morphological and structural properties of the NiM catalysts.

| Catalyst | $S_{BET}$ ($m^2g^{-1}$)[a] | Pore Volume ($cm^3g^{-1}$)[b] | Pore diameter (nm)[c] | NiO Crystallite size (Å)[d] |
|---|---|---|---|---|
| NiBa | 55 | 0.10 | 7.52 | 250 |
| NiCa | 125 | 0.13 | 4.17 | 229 |
| NiK | 125 | 0.17 | 5.54 | 230 |
| NiSr | 82 | 0.07 | 3.62 | 111 |

[a] calculated by BET equation
[b] BET adsorption pore volume
[c] BET adsorption average pore diameter (4V/A) and [d] average crystalline diameter using Scherrer equation from XRD.

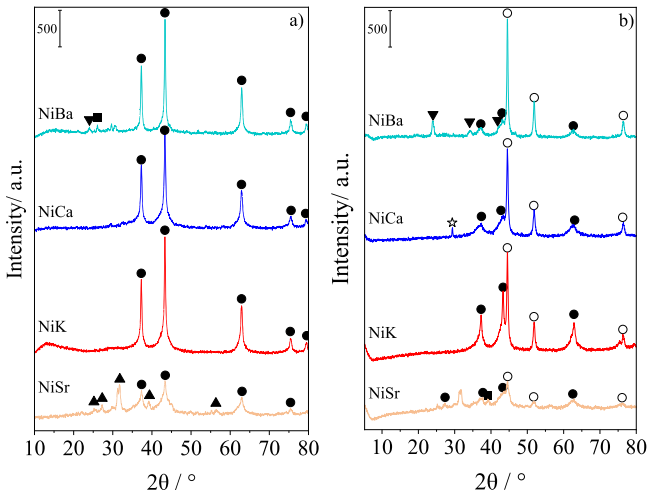


**Fig. 1.** XRD patterns of NiBa, NiCa, NiK and NiSr catalysts after a) calcination at 800 °C and b) a reduction treatment in 3 % hydrogen at 600 °C for 1 h. The ● symbol represents NiO, the ○ represents $Ni^0$, the ☆ represents $CaCO_3$, the ▼ represents $BaCO_3$, the ■ represents $SiO_2$ and the ▲ represents $Sr_2SiO_4$.

corresponding to the diffraction planes (111), (200), (220), and (311), respectively. Using the *Scherrer* equation, the average NiO crystallite size was calculated and included in Table 1. Interestingly, no additional oxide phases were observed in the high-temperature calcined NiBa, NiK, NiSr, and NiCa samples, suggesting that the incorporation of barium, calcium, strontium, or potassium does not result in the formation of distinct phases during the synthesis process. Minor signals corresponding to barium carbonate (ICDD n° 04–009–6036 and ICDD n° 04–016–3101) and silica ($SiO_2$, ICDD n° 00–016–0380) were detected in the NiBa catalyst. The diffraction profile of the NiSr catalyst exhibited notable differences in terms of crystallinity with broader Bragg peaks. A NiO crystallite size of 111 Å was estimated for NiSr, which is smaller than those calculated for the other catalysts, where the crystallite sizes are in the range of 229–250 Å. Additionally, strontium silicate (ICDD n° 04–013–5411) and strontium carbonate (ICDD n° 01–078–4340) were identified. The presence of silicates species is attributed to the incorporation of colloidal silica during the preparation process.

Fig. 1b shows the XRD patterns of the NiM catalysts after activation. The activation process involved reducing the catalysts for 1 h in a 3 % $H_2$/He stream at 600 °C. Once undergone activation, most of the NiO oxide peaks disappeared or their intensity were further reduced, and a cubic metallic Ni crystalline structure was observed at 44.5°, 51.86°, and 76.39° (ICDD n° 04–006–1675) for all NiM catalysts. This indicated that the thermal treatment with hydrogen at high temperature provokes the Ni-formation from its oxide form, resulting in a bulk catalyst where part of the nickel is present as metallic Ni supported on the remaining nickel oxide (Ni/NiO), as evidenced by the overlapping diffraction patterns associated to Ni and NiO structures. No reduction of side species carbonates or silicates was observed, although these signals were irrelevant for the NiBa, NiCa, NiK and NiSr catalysts.

The ratio of intensities associated with the X-ray diffraction (XRD) signals, resulting from the coexistence of Ni/NiO crystalline species after $H_2$ reduction, varies depending on the type of unsupported NiM catalyst used. In general, the incorporation of transition metals or alkaline metals can increase the reduction difficulty of NiO species because of the interaction between NiO and M [51]. This suggests that the addition of different metals—such as barium or alkali and alkaline earth metals—can influence the reduction of nickel oxide (NiO) to metallic nickel (Ni). Specifically, the presence of barium produces the highest Ni/NiO intensity ratio, with the majority diffraction signal for the reduced Ni phase being 7.6-times greater than that for the remaining NiO after activation in hydrogen. For the NiCa system, the intensity ratio was 4.6, while for potassium (NiK) and strontium (NiSr), the ratio is close to approximately 1.7. These findings indicate that barium and calcium facilitate the reduction process more effectively than potassium and strontium. This effect is likely due to an increase in electron density on the surface, which enhances the conversion of nickel oxide to metallic nickel. In contrast, nickel-bulk surface is less prone to reduction without the influence of alkali-or alkaline earth-metals.

Raman spectra of calcined unsupported catalysts are shown in Fig. 2. Undopped NiO bulk catalyst presented peaks at 400, 530, 730, 900, 1090 $cm^{-1}$ [52,53].

The prepared NiM catalysts features a primary band near 510 $cm^{-1}$ and a very weak band at 710 $cm^{-1}$, which are attributed to Ni–O stretching vibrational modes. A shoulder peak around 380 $cm^{-1}$ indicates the non-stoichiometry of NiO. For the NiM catalysts, signals recorded with maximun in the 505–514 $cm^{-1}$ range are associated with dispersed nickel oxide crystals and exhibit shifts in Raman intensity depending on the nature of the incorporated metal. Additionally, a less intense and broad signal corresponding to crystalline NiO were observed in the 780 to 1200 $cm^{-1}$ range. Compared to bulk-NiO, the peaks in the NiM samples are weaker and shift to higher frequencies, suggesting that an interaction occurred between NiO and the alkaline earth metal oxide during preparation. Another signal near 475 $cm^{-1}$, not present in pure NiO, can be attributed to the formation of BaO.NiO, $K_2O$.NiO, CaO.NiO or SrO.NiO side species linked to the vibrations of intermetallic surface species. For oxidized catalysts no signals were detected at 620 $cm^{-1}$, which are typically associated with surface oxygen vacancies. Ba, K, Ca, or Sr interact with the NiO species, modifying the intensities of both the 510 and 1100 $cm^{-1}$ modes. This interaction occurs at the surface level, particularly in supported catalysts or through metal intercalation into the NiO lattice. As seen in the XRD patterns, no signals related to other crystalline metallic oxides were detected, although some may not be Raman-active phases. However, certain carbonate crystalline phases, also observed in the XRD, should overlap with the NiO Raman region (505–516 $cm^{-1}$) in agreement R. E. Benner et al. was earlier reported [54]. Furthermore, for the $H_2$-activated catalyst treated at 600 °C for 1 h in a 3 % $H_2$/He atmosphere (Fig. 2b), Raman spectra exhibited an unusual flat profile, with a significant attenuation of the Ni-oxide-related modes. Ni does not show any peaks in the Raman spectrum as Ni face-centered cubic (FCC) metal has a single atom primitive unit cell and does not show any polarizability change due to the interaction between the electric field of the monochromatic light and dipole moment within the material [55]. The absence of Ni-related Raman signals cannot be attributed to an amorphization of the material. In its metallic form, particularly in the face-centered cubic (FCC) structure, nickel (Ni) does

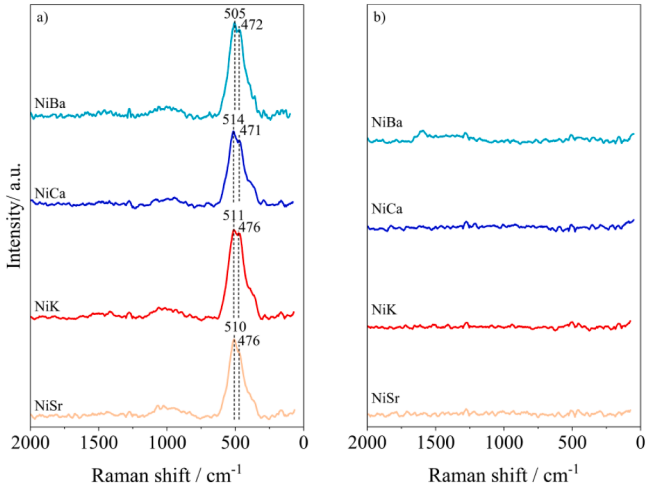


**Fig. 2.** Raman spectra of NiBa, NiCa, NiK and NiSr after a) calcination at 800 °C in air and b) a reduction treatment in 3 % hydrogen at 600 °C for 1 h.

not generate Raman signals, which is typical for metallic materials. These generally exhibit weaker Raman signals compared to the systems after calcination in air. When metallic Ni is present in a mixture with NiO, a complete disappearance of the Raman signals occurs.

The surface compositions and chemical valence states of the calcined catalysts were examined using X-ray photoelectron spectroscopy (XPS) and data are reflected in Table 2. The XPS spectra of the metallic elements (Ni, Ba, Ca, K, and Sr) were analyzed. The Ni $2p_{3/2}$ peak of NiM could be deconvoluted into two $Ni^{2+}$ signals near 855–856 eV, with a satellite signal at approximately 861 eV [54]. A notable shift in the peak maximum was observed upon incorporation of the second metal, which can be attributed to the differences in electronegativity between Ni (1.91 on the Pauling scale) and Ba (0.89), K (0.82), Ca (1.00), or Sr (0.95). The main Ni $2p_{3/2}$ peak shifted to higher binding energies, likely due to charge transfer from the alkaline metal to the adjacent Ni. This trend follows the electronegativity order: Ca>Sr>Ba for divalent cations. Potassium exhibited the largest shift, although it is the only monovalent cation. The Ba 4d spectrum indicated the presence of $Ba^{2+}$, with the core-level deconvolution revealing two binding energies corresponding to BaO and $BaO.CO_2$ -BaO.NiO [56]. Calcium and strontium, with a single signal, were predominantly present in their intermetallic oxide or their carbonated forms, being $CaO.CO_2$ and CaO.NiO for NiCa, and Sr-OH for NiSr catalyt [57], while potassium appeared as a oxide hydroxyl-hydroxycarbonate [58]. Table 2 also includes the Ni/M ratios calculated from ICP-MS analyses where the NiBa and NiK catalysts exhibited Ni/M ratios lower than the theoretical ratio set in the experimental section. This discrepancy suggests defective Ni loading, likely due to the slower precipitation kinetics of nickel, which may have been removed as $Ni^{2+}$ during washing steps [59]. In contrast, the NiCa and NiSr catalysts displayed ratios slightly greater than 10/1.

$H_2$-TPR consumption profiles of the Ni-based catalyst are shown in Fig. 3. $H_2$-TPR profile presented two main peak-range reduction maxima. Superimposed weaker peaks registered in the 350–500 °C range attributed to the reduction of small NiO particles interacting with the alkaline-alkaline earth species on the surface of unsupported catalysts; The maximum ca. 420 °C is attributed to $Ni^{+2}$ nano-spread mixed species reduction and related to the reduction of $Ni^{2+}$ to metallic Ni at surface of NiO to Ni ($Ni^{2+} \rightarrow Ni^0$) [60]. The different $H_2$-consumption registered for modified-NiO catalysts indicated that the MO.NiO intermetallic structures provoke T-shifts in the low range associated with multistep hydrogen consumption processes. A broad and progressively increasing $H_2$ consumption signal with a $T_{max}$ at 730–740 °C was attributed to the gradual interior-reduction of the main NiO bulk phase but may also involve additional hydrogen consumption by decarbonation of local carbonate species.

$CO_2$-TPD analysis was performed to identify the nature of basic surface sites for the synthetized catalysts and the results are presented in Fig. 4. In Fig. 4a) the $CO_2$ desorption profile expressed in ppm as a function of temperature is presented for the bimetallic unsupported catalysts. The catalysts presented desorption peaks in different temperature regions: the first signal of $CO_2$ desorption was observed in the range between the 100–300 °C and the second between 400–600 °C, which corresponds to weak and moderated to strong basic sites, respectively [61].

The $CO_2$-release detected for all the catalyst, as a very broad signal at temperatures lower than 300 °C are attributed to $CO_2$ chemisorption of weak basic sites. Moreover, a second and intense signal of $CO_2$ at 507 °C was detected only for NiCa catalyst that could be related to the presence of strong basic sites. According to the literature, the weak basic sites are attributed to linear adsorption of $CO_2$ whereas medium and strong basic sites are due to formation of stable bridged adsorption state of $CO_2$; $CO_2$ absorbed in weak basic sites is associated with monodentated carbonates and/or formate-species formation while $CO_2$ adsorbed on strong basic sites will be retained as monodentated carbonate species [62].

The electronegativity and alkaline character of the incorporated metals affect the basicity distribution by changing the $CO_2$ desorption temperature in the region of the weak basic sites (< 300 °C). It is observable a T-shifts from 135 to 150 °C as a narrow signal for NiCa and NiBa to a wide desorption $CO_2$ signal for NiSr or NiK catalysts. The increase of narrow to a wider distribution of weak basic sites from 135 to 150 °C is result of the interaction NiO and the metal oxide alkaline character incorporated. The amount of $CO_2$ is correlated with the number of basic sites of catalyst, it can be assumed that K and Sr addition leads to increase of weak basicity sites population, much higher than registered for the Ba and Ca. In addition, these weak basic sites are directly involved in adsorption of $CO_2$ and hence, an increase of weak sites population due to the alkaline metal nature affects potential $CO_2$ storage capacity.

Calculated $CO_2$ storage and desorption capacity values are presented in Table 3. $CO_2$-storage net capacity was calculated by numerical integration of a $CO_2$-He cycle at 600 °C, as was reported in the experimental section, and considering that part of $CO_2$ is retained and partially desorbed during the He purge step, such that the difference between $CO_2$ fed ($CO_2^{in}$ area) and [$CO_2^{adsorbed}$-$CO_2^{desorbed}$] determines the net retention capacity.

As can be seen, NiBa and NiSr presented lower values than NiK and NiCa ranging between 0.160 and 0.196 $mmolCO_2 \cdot g_{cat}^{-1}$; this fact can be attributed to the nature of Ca and K oxides and their abilities to storage $CO_2$ as carbonates or hydrogen-carbonates stable species. The values are lower than those found in the literature for adsorbents for $CO_2$-capture from flue gas [63], thus, MgO typically used as sorbent for $CO_2$ capture has a maximum capture capacity close to 8.2 mg $CO_2 \cdot g_{adsorbent}^{-1}$ [64] or CaO using in calcium looping technology presented the highest adsorption capacity (0.38 g $CO_2 \cdot g_{adsorbent}^{-1}$) but its stability is poor due to sintering and diffusion of $CO_2$ through the $CaCO_3$ layer formed on the surface [65]. However, these catalysts are developed for their use in storage and regeneration alternating cycles operation instead of as $CO_2$-adsorbent materials. Based on the amount of $CO_2$ adsorbed (Table 3) registered at 600 °C catalyst were ranked in the following order: NiCa=NiK>NiBa>NiSr associated with the basic-sites population. It should be noted that the amount desorbed throughout the temperature range is considerably lower than the retention capacity of these materials and following the order Ca>*K*>>Ba>Sr. Calcium desorbs practically 65 % of the $CO_2$ retained between 350–600 °C associated with strong basic sites that are not detected in the rest of the catalysts.

Due the interaction of $CO_2$ with those alkaline oxide-modified Ni-based catalysts the CO formation is often-overlooked during the $CO_2$-TPD. The small fraction of CO desorbed is also correlated with the population of basic sites and the signals at medium temperature range are also observed, with CO-$T_{max}$ peaks between 350–600 °C. The highest intensity CO-signals correspond to NiK with a maximum of 544 °C. For NiCa catalyst a medium signal in the 400–600 °C range was registered. For NiBa, CO formation shifts to lower temperature with a maximum at 407 °C. No CO signal was detected for NiSr catalyst. CO formation

**Table 2**
XPS data resume and Ni/M ratio of calcined samples at 800 °C.

| Catalyst | Ni $2p_{3/2}$ | | Alkaline metal | | | Ni/M[a] |
|---|---|---|---|---|---|---|
| | B. E. (eV.) | Species | Region | B. E. (eV.) | Species | |
| NiBa | 855.1<br>861.1 | $Ni^{+2}$<br>$Ni^{+2}$ sat. | Ba $4d_{5/2}$ | 87.9<br>89.9 | BaO<br>$BaO.CO_2$<br>BaO.NiO | 9 |
| NiCa | 855.5<br>861.6 | $Ni^{+2}$<br>$Ni^{+2}$ sat. | Ca $2p_{3/2}$ | 346.4 | $CaO.CO_2$<br>CaO.NiO | 11 |
| NiK | 855.9<br>861.8 | $Ni^{+2}$<br>$Ni^{+2}$ sat. | K $2p_{3/2}$ | 294.5 | $K_4H_2(CO_3)_3 \cdot 1.5H_2O$ | 8 |
| NiSr | 855.2<br>861.4 | $Ni^{+2}$<br>$Ni^{+2}$ sat. | Sr $3d_{5/2}$ | 132.9 | $SrO.CO_2$<br>Sr-OH*<br>*$[Sr(OH)_2 \cdot 8H_2O]$ | 12 |

[a] from ICP-MS measurements.

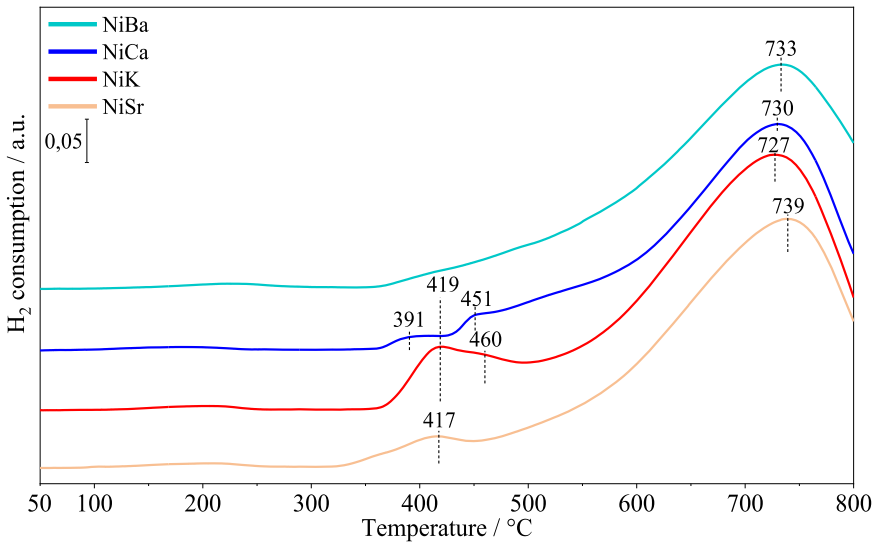


**Fig. 3.** $H_2$-TPR profiles of the calcined bimetallic unsupported catalysts.

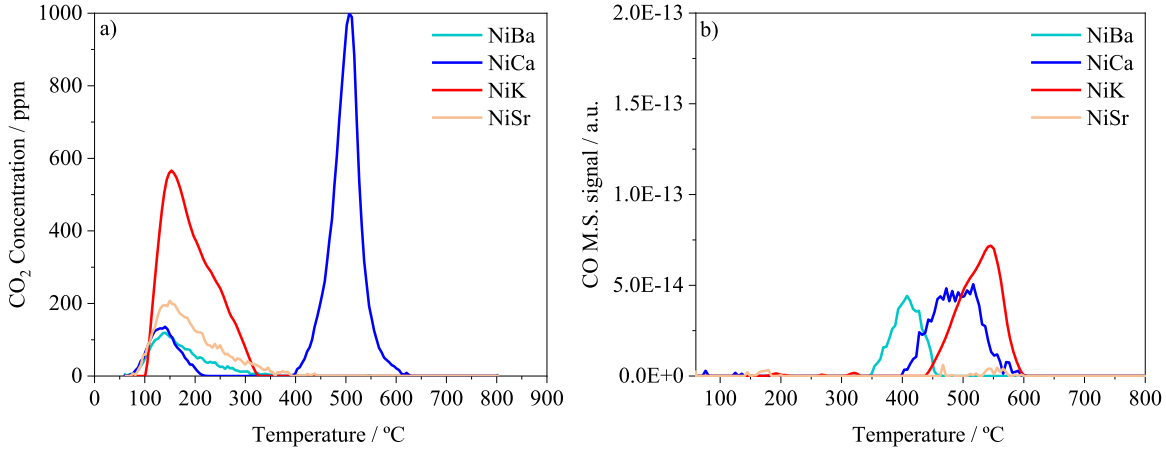


**Fig. 4.** a) $CO_2$ concentration profile and b) MS-signal of CO obtained from the $CO_2$-TPD measurements.

**Table 3**
$CO_2$-storage capacity calculated from the accumulation step at 600 °C and desorption capacity calculated from total $CO_2$-TPD measurements.

| Catalyst | Adsorption capacity at 600 °C* $mmolCO_2 \cdot gcat^{-1}$ | Desorption Capacity (25–800 °C)** $\mu mCO_2 \cdot gcat^{-1}$ |
|---|---|---|
| NiBa | 0.171 | 6.4 |
| NiCa | 0.196 | 35.2 |
| NiK | 0.197 | 31.6 |
| NiSr | 0.160 | 13.3 |

* From saturation curve at 600 °C.
** From $CO_2$-TPD.

during $CO_2$ desorption in inert atmosphere must be related to redox properties modification by presence of alkaline or alkaline earth during thermal reduction of $CO_2$. The trend observed in XPS of the decrease in the value of the nickel oxide binding energy due to interaction with the incorporated metals follows the order Ba<Ca<*K*; which coincides with the order of temperatures at which the reduction of $CO_2$ occurs by detection of CO. Moreover, the origin of CO formation on these unsupported catalysts is related to the coexistence of NiO and Ni-metallic species that play a role favoring the formation of CO by decomposition of adsorbed $CO_2$. $CO_2$ storage is increased due to carbonates and bicarbonates formation, this last promoted by strong- hydroxyl surface groups; so, the release of CO at high temperature, and $CO_2$, is further evident for K and Ca oxides in correlation to overall basicity.

Although the $CO_2$ adsorption capacity determined by isothermal measurements at 600 ºC provides valuable insight into the availability of basic sites, it does not fully account for the catalytic performance observed under $CO_2$-SR cyclic conditions. The $CO_2$ removal efficiency and product distribution are influenced not only by the density and strength of surface basic sites, but also by the redox properties of the Ni–M systems, which govern the activation of stored species and the regeneration of active sites during the $CH_4$ step. Therefore, the apparent discrepancy between the $CO_2$ adsorption trend (NiCa ≈ NiK > NiBa > NiSr) and the catalytic activity ranking (NiBa > NiCa > NiK > NiSr) reflects the multifactorial nature of the process, where reactivity is determined by the interplay of basicity, reducibility, and the dynamics of oxygen transfer at the Ni–MO interface.

### 3.2. *Comparative activity in $CO_2$-SR alternated-cyclic technology*

Recently, our research group developed a novel technology based on the LNT-NOx methodology, adapted to operate in alternating stages [48, 49]. This process involves the capture of a $CO_2$ stream (in the absence of $NO_x$ or other contaminants), simulating its presence in an industrial combustion effluent, and its chemical revalorization into hydrogen-rich syngas through an in-situ methane reforming step. This dual-function

cycle is referred to as $CO_2$-storage–regeneration ($CO_2$-SR) technology.

This technology takes the advantage of the chemical loop process, where two greenhouse gases as $CH_4$ and $CO_2$ are fed separately, thereby overcoming the limitations imposed by equilibrium conversion rates in the co-feed mode. This strategy combines $CO_2$ capture and subsequent reduction in a single process with two distinct steps: (i) the capture of $CO_2$ on a storage component of the catalyst and (ii) the release of $CO_2$ and direct catalytic reaction of stored $CO_2$ by a reducing gas ($CH_4$), with the simultaneous catalyst regeneration promoted by the metallic component (Ni) of the catalyst. These alternated phases operated isothermally.

This study examined how the incorporation of barium, calcium, potassium and strontium influences the lattice structure of the unconventional bimetallic NiM unsupported catalysts. The performance of the unsupported catalysts was evaluated at 600 °C.

The isothermal alternated cyclic performance of NiBa, NiCa, NiK and NiSr catalysts in the $CO_2$ storage and regeneration process was evaluated, feeding $CO_2$-He and $CH_4$-He pulses (10,000 ppm each one and GHSV of $2.12x10^4\ h^{-1}$) with an intermediate purge of He, using Ar as a tracer at 600 °C and ordinary pressure. Catalysts were previously reduced *in situ* at 600 °C under hydrogen atmosphere. In Fig. 5, the concentration profiles of $CO_2$, $CH_4$, CO, $H_2$ at the reactor outlet for a representative cycle are represented. The ion-current of $H_2O$-signal appears to be perturbed during the whole experiment and unfortunately, the peak-shape was not well-defined inside of pulse-width and consequently was not included in the figures, as well as the signal associated with the square pulse of the Ar. It is worth mentioning that for NiBa catalyst, the steady-state is reached after the third-fourth operation cycle, for NiK and NiSr a similar behavior was observed, whereas NiCa did not present a stable performance and the data represented in Fig. 5 corresponds also to the fourth cycle. Additionally, for each catalyst, $CO_2$ removed in the storage step and $CH_4$ conversion and $H_2$/CO ratios during the regeneration phase calculated in the cycles represented in Fig. 5 are shown in Table 4.

During the $CO_2$-storage step, the typical $CO_2$ saturation profile was observed along with the production of CO. The first difference observed for NiM catalysts is the time in which $CO_2$ saturation is reached. For the feeding of 10,000 $ppm_v$ of $CO_2$, the time of saturation follows the trend NiCa>NiBa>NiK=NiSr, since for NiBa, $CO_2$ saturation is achieved within 2–3 min, 3–4 min are needed for NiCa and 1–2 min for NiK and NiSr. CO was detected from the very first time on the cycle, reaching a maximum which is closely dependent on the NiM catalyst and falling to zero at the end of the $CO_2$ pulse. Besides, a slight evolution of the baseline of the signal associated with hydrogen can be seen and is

**Table 4**
Activity values of NiM catalysts in terms of $CO_2$ removed, $CH_4$ converted and selectivity as $H_2$/CO ratio for a representative cycle performed at 600 °C.

| Catalyst | % $CO_2^{removed}$ * | % $CH_4^{conv}$ ** | $H_2$/CO** |
|---|---|---|---|
| **NiBa** | 2.15 | 3.40 | 19 |
| **NiCa** | 2.64 | 3.52 | 19 |
| **NiK** | 1.56 | 2.57 | 5 |
| **NiSr** | 1.53 | 2.17 | 8 |

* During the adsorption step.
** During the regeneration step.

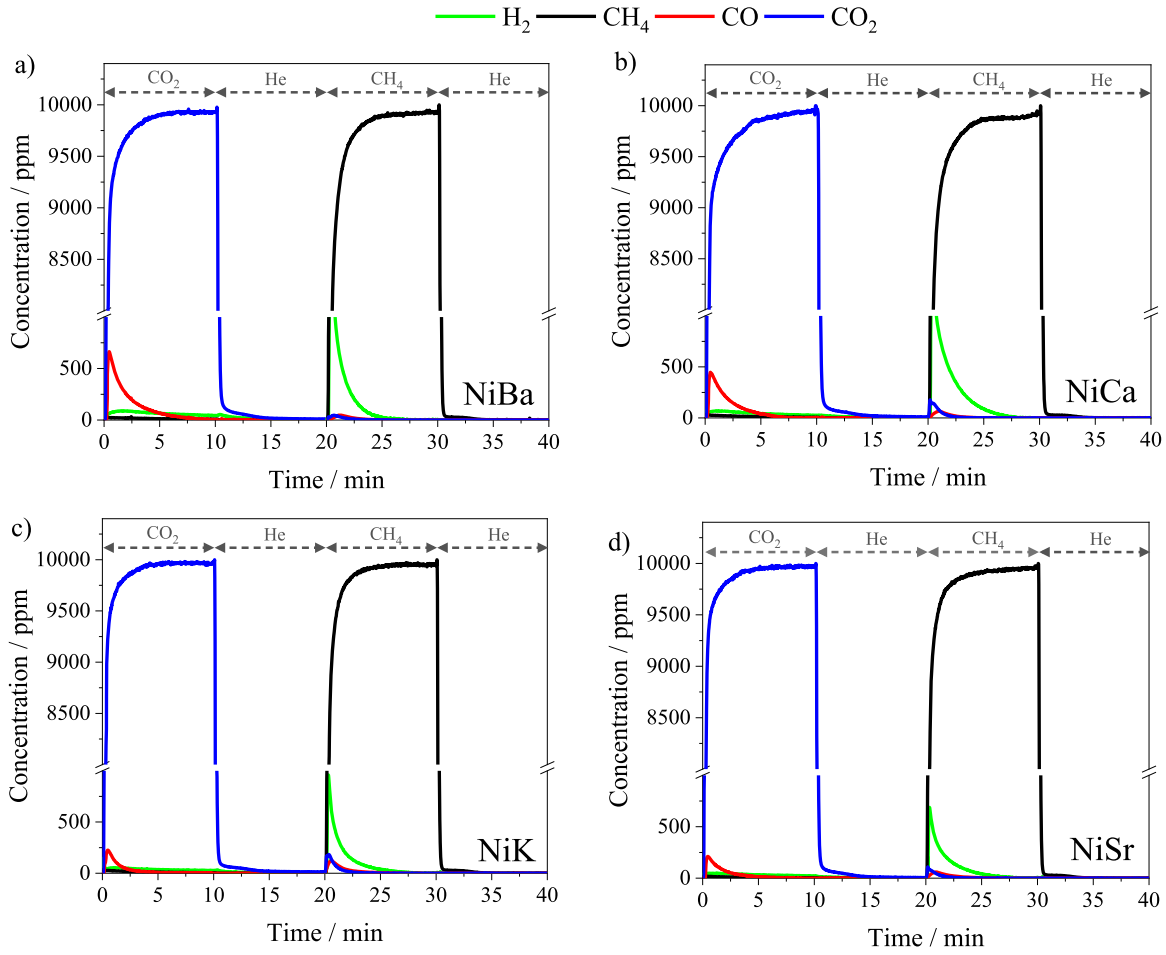


**Fig. 5.** $CO_2$, $H_2$, $CH_4$ and CO concentration profiles during alternating cycles of $CO_2$ adsorption and $CH_4$ regeneration with 10 min He purges over the catalysts a) NiBa, b) NiCa, c) NiK and d) NiSr.

related to the presence of hydrogen traces due to the previous $CH_4$-step.

In the regeneration step using methane (as a reducing and regenerating agent), methane at the outlet was recorded, indicating an initial consumption that depends on the catalyst used. The evolution of the signals associated with $H_2$, $CO_2$ and CO was also registered during this pulse. Hydrogen was the main product detected, in concentrations higher than $CO_2$ and CO, which are almost coincident, and with maximums that depended on the alkaline or alkaline-earth incorporated in the formulation, being similar for K and Sr and much higher for Ba and Ca. Low CO formation and $CO_2$ production may be due to reforming reactions and desorption.

At 600 °C, the values of $CO_2$ and $CH_4$ conversions are presented in Table 4. The values of $CO_2$ removed should be understood as the sum of $CO_2$ stored and converted since the data were obtained as was explained in the experimental section from the differences between inlet and outlet $CO_2$ mass signals.

$CO_2$ removal capacity for NiBa and NiCa, with values of 2.15 and 2.64 %, was higher than those values observed for NiK and NiSr, 1.56 and 1.53 %, respectively. These values are in agreement with the saturation period observed at the beginning of the $CO_2$ storage step of the cycle but not exactly with the adsorption capacity or basicity of the catalysts tabulated in Table 3, in which NiK and NiCa systems are those with the highest adsorption capacities measured at 600 °C, indicating that the activity in the storage stage does not depend only on the $CO_2$ retention capacity of the catalyst. The reactivity of the alkaline or alkaline earth metal is what controls the $CO_2$ removal capacity achieved, which could be related to the redox behaviour of the catalysts. Calcium is often used in Looping Dry Reforming of Methane (CaLDRM) since it could realize $CO_2$ capture and *in-situ* valorization into syngas [66] and barium is used as model catalyst [49]. Moreover, during the regeneration step, $CH_4$ conversion values are always higher than $CO_2$ values for all the catalysts tested, indicating other reactions involved in contrast of those reported by single $CO_2$-reforming reaction [9,37,67]. Additionally, the $H_2$/CO ratios are higher than expected, especially for NiBa and NiCa; this deviation has been attributed to the contribution of other side reactions. Methane decomposition as parallel reaction causes the increase in hydrogen production above the stoichiometric value for methane reforming with $CO_2$. The extent of these reactions depends on the nature of the metal incorporated into the unsupported bimetallic catalyst. The reaction scheme for both $CO_2$ storage and $CH_4$ regeneration steps was outlined in previous studies [48,49] for the NiBa catalyst. Given that the same component distribution was detected in the gas-off stream, shown in Fig. 5, it is assumed that the reaction network remains similar, although the possibility of additional reactions cannot be excluded.

In the case of NiM catalysts, $CO_2$ storage occurs on Ba, Ca, K or Sr basic sites. Meanwhile, $CH_4$ conversion takes place at Ni-reduced mixed centers, involving the $CO_2$ saturated sites. The rate-limiting step is the reaction between the $CO_2$-storage centers and $CH_4$, which leads to the production of $H_2$ and CO through mainly dry reforming reaction of methane and the regeneration of metal and basic sites. $CO_2$-storage, involving heterometallic mixed-centers Ni-MO, and the production of CO and $H_2$ can be explained taking into account four different reactions, depending on the phase in the cycle and can be described by the 6–10 equations: activated $CO_2$ decomposition (Eq. (6)), methane dry reforming DRM (Eq. (7)), $CO_2$-carbon gasification (Eq. (8)), the internal reverse water-gas shift, RWGS as (Eq. (9)) and methane decomposition (Eq. (10)) contribution as co-side reaction.

$$2CO_2\ (cat) \rightarrow CO_2^{sto} + CO\ (g) + O^* \quad (6)$$

$$CO_2^{sto} + CH_4 \rightarrow 2CO\ (g) + 2H_2\ (g) \quad (7)$$

$$CO_2\ (g) + C\ (s) \leftrightarrow 2CO\ (g) \quad (8)$$

$$CO_2\ (g) + H_2\ (g) \rightarrow CO\ (g) + H_2O\ (g) \quad (9)$$

$$CH_4\ (s) \leftrightarrow C\ (s) + 2H_2\ (g) \quad (10)$$

To further compare the influence of alkaline or alkaline-earth on the occurrence of these reactions, the production of CO in both storage and regeneration steps has been analyzed. In Fig. 6 the CO concentration in ppm for NiM catalysts are presented. During the $CO_2$-storage step, an instant CO formation with a sharp signal is detected which is related to the occurrence of two parallel reactions: the reaction between $CO_2$ with the deposited carbon (C(s)) species through gasification reaction (Eq. (8)) and the dissociative decomposition reaction of $CO_2$ adsorbed on the basic sites (Eq. (6)). That was confirmed for a similar NiBa catalyst by labeled $^{13}CO_2$ experiment [49]. There is a notable difference in the CO concentration attributable to the second metal added to Ni. A higher CO concentration was observed for both NiBa and NiCa, as a consequence of a major extension of the gasification reaction with more carbon deposited according to the methane conversion values during the regeneration stage, shown in Table 4. The contribution to CO formation from the decomposition reaction of stored $CO_2$ cannot be ruled out and would be related to the lower temperature of CO formation as was registered in the TPD-$CO_2$ experiments shown in Fig. 4b. During the regeneration step, the amount of CO produced for all catalysts is an order of magnitude lower than those registered during the storage period. CO is produced by the dry reforming reaction of methane (Eq. (7)) without ruling out that, although the system is working in dry conditions, the water generated by parallel reactions could react with the methane fed through the steam reforming reaction (Eq. (11)). In particular, NiK presented the highest value and therefore the lowest $H_2$/CO ratios; the high CO concentration can be associated with the presence of a partially hydroxylated potassium surface in the form of hydroxycarbonates highly reactive and able to perform the reaction presented in Eq. (12).

$$CH_4\ (g) + H_2O\ (cat) \leftrightarrow CO\ (g) + 3H_2\ (g) \quad (11)$$

$$CH_4\ (g) + OH* \leftrightarrow CO\ (g) + 5/2H_2\ (g) \quad (12)$$

Although all bimetallic developed catalysts are active in the reactions described for the overall behaviour in the $CO_2$-SR technology, a clear enhanced catalytic activity for the systems containing Ba and Ca was registered in terms of $CO_2$ and $CH_4$ conversion values and even $H_2$/CO ratios, producing a $H_2$-enriched stream in the outlet gas. NiBa catalyst exhibits lower $CO_2$ adsorption and desorption capacities compared to NiCa and NiK (as shown in Table 3 and Fig. 4), its superior performance under cyclic $CO_2$-SR conditions can be attributed to its enhanced redox properties and surface reactivity. As evidenced by the $H_2$-TPR profiles, NiBa presents the highest reducibility among the tested catalysts, facilitating the activation of stored $CO_2$ and promoting

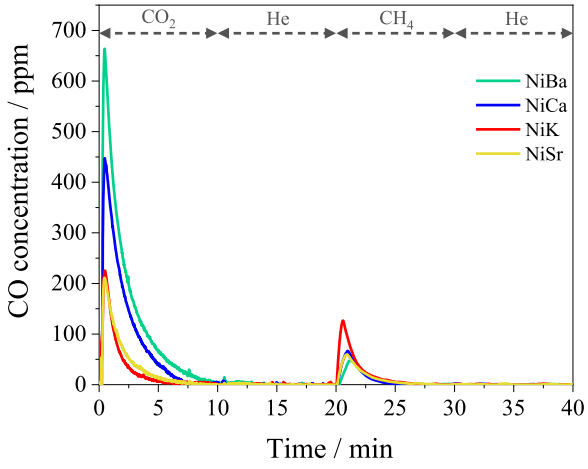


**Fig. 6.** CO concentration profiles during alternating cycles of $CO_2$ adsorption and $CH_4$ regeneration with 10 min He purges over NiBa, NiCa, NiK and NiSr catalysts.

effective regeneration with $CH_4$. Furthermore, the presence of Ba-containing species such as BaO·NiO and $BaCO_3$ provides moderate basic sites capable of both capturing and activating $CO_2$ in a reactive form. This highlights that, beyond the static $CO_2$ storage capacity, the dynamic redox behavior and oxygen transfer ability of the catalyst play a decisive role in the overall performance of the $CO_2$-SR cycle. Another important property for the catalytic activity of alternating cycles is stability, which has been addressed as repeatability in terms of $CO_2$ removal capacity, by conversion or storage. Thus, Fig. 7 shows the $CO_2$ conversion during four consecutive and alternating cycles for the NiCa and NiBa catalysts, which are overall the most active. While for the bimetallic catalyst NiBa the $CO_2$ removal value remains constant slightly above 2 %, the $CO_2$ conversion value for the NiCa catalyst progressively decreases to 1.5 %, which are the average values obtained for the catalysts containing K and Sr. This decrease is due to methane is not able to completely regenerate the catalyst surface at 600 °C because of the formation of stable calcium carbonates is increased with the consecutive cycles. Therefore, NiCa system would need a stronger reductant agent or higher operating temperature for the thermodynamic reversibility of $CaO/CaCO_3$ system in agreement with J. Hu et al. [66].

The 1/10 promoter M/Ni ratio in the catalyst was selected based on previous results that suggested that these concentrations of alkali metals can help to not only to enhance and control the selectivity in the $CO_2$-SR technology via alkali metal−Ni interaction but also to the generation of reactive-oxygen species due to incorporation of alkali in the NiO-lattice. The unsupported bimetallic catalytic material developed possess dual functionality: adsorption-storage and chemical regeneration capabilities. This study has shown that the incorporation of alkaline or alkaline-earth elements modifies the capacity for $CO_2$ retention and regeneration with methane at high temperatures, producing different concentrations of CO in both stages and hydrogen-enriched streams when methane is fed. This is associated with the fact that the interaction of alkaline or alkaline-earth metal with nickel causes the modification of the population of NiO.MO centers and the reducibility of the material, which is directly associated with the activity in cyclic storage and regeneration technology. The reaction route is maintained; however, the extent of the reactions is a function of the second element incorporated.

This work provides new insights into the design of bifunctional unsupported catalysts for $CO_2$ storage and reduction co-aided by the incorporation of an active alkaline or alkaline-earth metal component.

## 4. Conclusions

Highly innovative dual function catalytic materials aim to facilitate the production of syngas from industrial flue gas emissions, $CO_2$ and $CH_4$, working in alternating-cyclic operation conditions. The role of alkaline and alkaline-earth metal was addressed in a set of NiM catalyst synthetized, characterized and tested in the $CO_2$-SR technology, where M are Ba, Ca, K and Sr. $CO_2$ removal capacity for NiBa and NiCa, with values of 2.15 and 2.64 %, was higher than those values observed for NiK and NiSr, 1.56 and 1.53 %, respectively. Methane conversion is always higher than carbon dioxide conversion and a complex set of reaction was described including, reforming, carbon gasification mainly. Otherwise, barium and calcium facilitate the reduction process more effectively than potassium and strontium. This effect is likely due to an increase in electron density on the surface, which enhances the conversion of nickel oxide to metallic nickel.

## CRediT authorship contribution statement

**Sofía Essounani-Mérida:** Data curation, Investigation, Methodology, Writing – original draft. **Sergio Molina-Ramírez:** Data curation, Investigation, Methodology. **Marina Cortés-Reyes:** Data curation, Formal analysis, Investigation, Methodology, Validation, Writing – review & editing. **Concepción Herrera:** Conceptualization, Formal analysis, Funding acquisition, Investigation, Project administration, Writing – original draft, Writing – review & editing. **Mª Ángeles Larrubia:** Conceptualization, Formal analysis, Funding acquisition, Investigation, Project administration, Supervision, Writing – review & editing. **Luis J. Alemany:** Conceptualization, Data curation, Formal analysis, Investigation, Methodology, Supervision, Validation, Writing – review & editing.

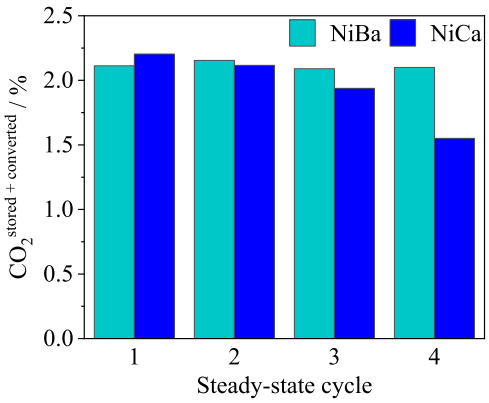


**Fig. 7.** $CO_2$ removal values for NiBa and NiCa catalysts during alternating steady-state cycles of $CO_2$ adsorption and $CH_4$ regeneration at 600 °C.

## Declaration of competing interest

The authors declare that they have no known competing financial interests or personal relationships that could have appeared to influence the work reported in this paper.

## Acknowledgement

The authors would like to acknowledge the financial support of PID2021-124098OB-I00 Project from the Ministry of Science, Innovation and Universities.

## Data availability

Data will be made available on request.

## References

[1] U.S. Energy Information Administration, Monthly energy Review- December 2019, (2019). https://biomassmurder.org/docs/2019-03-05-eia-annual-energy-outlook-2019-with-projections-to-2050-english.pdf.
[2] C.A. Horowitz, Paris agreement, Int. Leg. Mater. 55 (2016) 740–755, https://doi.org/10.1017/S0020782900004253.
[3] United Nations, Summary of Global Climate Action at COP29, (2025). https://unfccc.int/documents/644497.
[4] IEA, Net zero roadmap: a global pathway to keep the 1.5°C goal in reach, (2023).
[5] G. Centi, E.A. Quadrelli, S. Perathoner, Catalysis for $CO_2$ conversion: a key technology for rapid introduction of renewable energy in the value chain of chemical industries, Energy Environ. Sci. 6 (2013) 1711, https://doi.org/10.1039/c3ee00056g.
[6] P. Djinović, I.G. Osojnik Črnivec, B. Erjavec, A. Pintar, Influence of active metal loading and oxygen mobility on coke-free dry reforming of Ni–Co bimetallic catalysts, Appl. Catal. B Environ. 125 (2012) 259–270, https://doi.org/10.1016/j.apcatb.2012.05.049.
[7] K. Zhao, F. He, Z. Huang, G. Wei, A. Zheng, H. Li, Z. Zhao, Perovskite-type oxides $LaFe_{1-x}Co_xO_3$ for chemical looping steam methane reforming to syngas and hydrogen co-production, Appl. Energy 168 (2016) 193–203, https://doi.org/10.1016/j.apenergy.2016.01.052.
[8] H.A. Lara-García, D.G. Araiza, M. Méndez-Galván, S. Tehuacanero-Cuapa, A. Gómez-Cortés, G. Díaz, Dry reforming of methane over nickel supported on Nd–ceria: enhancement of the catalytic properties and coke resistance, RSC Adv. 10 (2020) 33059–33070, https://doi.org/10.1039/D0RA05761D.
[9] M. García-Diéguez, C. Herrera, M.Á. Larrubia, L.J. Alemany, $CO_2$-reforming of natural gas components over a highly stable and selective $NiMg/Al_2O_3$ nanocatalyst, Catal. Today 197 (2012) 50–57, https://doi.org/10.1016/j.cattod.2012.06.019.

[10] M. García-Diéguez, I.S. Pieta, M.C. Herrera, M.A. Larrubia, L.J. Alemany, RhNi nanocatalysts for the $CO_2$ and $CO_2$+ $H_2O$ reforming of methane, Catal. Today 172 (2011) 136–142, https://doi.org/10.1016/j.cattod.2011.02.012.

[11] M. García-Diéguez, M.C. Herrera, I.S. Pieta, M.A. Larrubia, L.J. Alemany, NiBa catalysts for $CO_2$-reforming of methane, Catal. Commun. 11 (2010) 1133–1136, https://doi.org/10.1016/j.catcom.2010.06.008.

[12] L. Azancot, L.F. Bobadilla, M.A. Centeno, J.A. Odriozola, IR spectroscopic insights into the coking-resistance effect of potassium on nickel-based catalyst during dry reforming of methane, Appl. Catal. B Environ. 285 (2021) 119822, https://doi.org/10.1016/j.apcatb.2020.119822.

[13] S.M. Kim, P.M. Abdala, M. Broda, D. Hosseini, C. Copéret, C. Müller, Integrated $CO_2$ capture and conversion as an efficient process for fuels from greenhouse gases, ACS Catal. 8 (2018) 2815–2823, https://doi.org/10.1021/acscatal.7b03063.

[14] S. Tian, F. Yan, Z. Zhang, J. Jiang, Calcium-looping reforming of methane realizes *in situ* $CO_2$ utilization with improved energy efficiency, Sci. Adv. 5 (2019) eaav5077, https://doi.org/10.1126/sciadv.aav5077.

[15] F. Nocito, A. Dibenedetto, Atmospheric $CO_2$ mitigation technologies: carbon capture utilization and storage, Curr. Opin. Green Sustain. Chem. 21 (2020) 34–43, https://doi.org/10.1016/j.cogsc.2019.10.002.

[16] F. Hussin, M.K. Aroua, Recent trends in the development of adsorption technologies for carbon dioxide capture: a brief literature and patent reviews (2014–2018), J. Clean. Prod. 253 (2020) 119707, https://doi.org/10.1016/j.jclepro.2019.119707.

[17] J. Hu, P. Hongmanorom, V.V. Galvita, Z. Li, S. Kawi, Bifunctional Ni-Ca based material for integrated $CO_2$ capture and conversion via calcium-looping dry reforming, Appl. Catal. B Environ. 284 (2021) 119734, https://doi.org/10.1016/j.apcatb.2020.119734.

[18] Y. Wang, P. Hu, J. Yang, Y.A. Zhu, D. Chen, C–H bond activation in light alkanes: a theoretical perspective, Chem. Soc. Rev. 50 (2021) 4299–4358, https://doi.org/10.1039/D0CS01262A.

[19] D. Pinto, V. Van Der Bom Estadella, A. Urakawa, Mechanistic insights into the $CO_2$ capture and reduction on K-promoted $Cu/Al_2O_3$ by spatiotemporal methodologies, Catal. Sci. Technol. 12 (2022) 5349–5359, https://doi.org/10.1039/D2CY00228K.

[20] Y. Kim, H.S. Lim, H.S. Kim, M. Lee, J.W. Lee, D. Kang, Carbon dioxide splitting and hydrogen production using a chemical looping concept: a review, J. $CO_2$ Util. 63 (2022) 102139, https://doi.org/10.1016/j.jcou.2022.102139.

[21] C. De Leeuwe, W. Hu, J. Evans, M. Von Stosch, I.S. Metcalfe, Production of high purity $H_2$ through chemical-looping water–gas shift at reforming temperatures – The importance of non-stoichiometric oxygen carriers, Chem. Eng. J. 423 (2021) 130174, https://doi.org/10.1016/j.cej.2021.130174.

[22] F. Massa, E.M. Cepollaro, S. Cimino, A. Coppola, F. Scala, Fluidized bed chemical looping for $CO_2$ capture and catalytic methanation using dual function materials, Proc. Combust. Inst. 40 (2024) 105648, https://doi.org/10.1016/j.proci.2024.105648.

[23] C. Zhang, Y. Li, Z. Chu, Y. Fang, K. Han, Z. He, Analysis of integrated $CO_2$ capture and utilization via calcium-looping *in-situ* dry reforming of methane and Fischer-Tropsch for synthetic fuels production, Sep. Purif. Technol. 329 (2024) 125109, https://doi.org/10.1016/j.seppur.2023.125109.

[24] M.A. Arellano-Treviño, Z. He, M.C. Libby, R.J. Farrauto, Catalysts and adsorbents for $CO_2$ capture and conversion with dual function materials: limitations of Ni-containing DFMs for flue gas applications, J. $CO_2$ Util. 31 (2019) 143–151, https://doi.org/10.1016/j.jcou.2019.03.009.

[25] S. Cimino, F. Boccia, L. Lisi, Effect of alkali promoters (Li, Na, K) on the performance of $Ru/Al_2O_3$ catalysts for $CO_2$ capture and hydrogenation to methane, J. $CO_2$ Util. 37 (2020) 195–203, https://doi.org/10.1016/j.jcou.2019.12.010.

[26] L.P. Merkouri, J.L. Martín-Espejo, L.F. Bobadilla, J.A. Odriozola, A. Penkova, T. Ramirez Reina, M.S. Duyar, Unravelling the $CO_2$ capture and conversion mechanism of a $NiRu–Na_2O$ switchable dual-function material in various $CO_2$ utilisation reactions, J. Mater. Chem. A 11 (2023) 13209–13216, https://doi.org/10.1039/D3TA01892J.

[27] A. Bermejo-López, B. Pereda-Ayo, J.A. González-Marcos, J.R. González-Velasco, Mechanism of the $CO_2$ storage and *in situ* hydrogenation to $CH_4$. Temperature and adsorbent loading effects over $Ru-CaO/Al_2O_3$ and $Ru-Na_2CO_3/Al_2O_3$ catalysts, Appl. Catal. B Environ. 256 (2019) 117845, https://doi.org/10.1016/j.apcatb.2019.117845.

[28] H. Sun, Y. Zhang, S. Guan, J. Huang, C. Wu, Direct and highly selective conversion of captured $CO_2$ into methane through integrated carbon capture and utilization over dual functional materials, J. $CO_2$ Util. 38 (2020) 262–272, https://doi.org/10.1016/j.jcou.2020.02.001.

[29] B. Nematollahi, M. Rezaei, M. Khajenoori, Combined dry reforming and partial oxidation of methane to synthesis gas on noble metal catalysts, Int. J. Hydrog. Energy 36 (2011) 2969–2978, https://doi.org/10.1016/j.ijhydene.2010.12.007.

[30] D. Pakhare, J. Spivey, A review of dry ($CO_2$) reforming of methane over noble metal catalysts, Chem. Soc. Rev. 43 (2014) 7813–7837, https://doi.org/10.1039/C3CS60395D.

[31] W.J. Jang, J.O. Shim, H.M. Kim, S.Y. Yoo, H.S. Roh, A review on dry reforming of methane in aspect of catalytic properties, Catal. Today 324 (2019) 15–26, https://doi.org/10.1016/j.cattod.2018.07.032.

[32] D. Wang, P. Littlewood, T.J. Marks, P.C. Stair, E. Weitz, Coking can enhance product yields in the dry reforming of methane, ACS Catal. 12 (2022) 8352–8362, https://doi.org/10.1021/acscatal.2c02045.

[33] T.Y. Liang, C.Y. Lin, F.C. Chou, M. Wang, D.H. Tsai, Gas-phase synthesis of Ni–CeOx hybrid nanoparticles and their synergistic catalysis for simultaneous reforming of methane and Carbon20Dioxide to Syngas, J. Phys. Chem. C (2018), https://doi.org/10.1021/acs.jpcc.8b00665. ACS Publ.s001.

[34] L. Lyu, M. Shengene, Q. Ma, J. Sun, X. Gao, H. Fan, J. Zhang, T.S. Zhao, Synergy of macro-meso bimodal pore and Ni-Co alloy for enhanced stability in dry reforming of methane, Fuel 310 (2022) 122375, https://doi.org/10.1016/j.fuel.2021.122375.

[35] D.G. Araiza, D.G. Arcos, A. Gómez-Cortés, G. Díaz, Dry reforming of methane over $Pt-Ni/CeO_2$ catalysts: effect of the metal composition on the stability, Catal. Today 360 (2021) 46–54, https://doi.org/10.1016/j.cattod.2019.06.018.

[36] A. Al-Mamoori, A.A. Rownaghi, F. Rezaei, Combined capture and utilization of $CO_2$ for Syngas production over dual-function materials, ACS Sustain. Chem. Eng. 6 (2018) 13551–13561, https://doi.org/10.1021/acssuschemeng.8b03769.

[37] H. Sun, Q. Zhang, J. Wen, T. Tang, H. Wang, M. Liu, P. Ning, L. Deng, Y. Shi, Insight into the role of CaO in coke-resistant over Ni-HMS catalysts for $CO_2$ reforming of methane, Appl. Surf. Sci. 521 (2020) 146395, https://doi.org/10.1016/j.apsusc.2020.146395.

[38] C.J. Liu, J. Ye, J. Jiang, Y. Pan, Progresses in the preparation of coke resistant Ni-based catalyst for steam and $CO_2$ reforming of methane, ChemInform 42 (2011), https://doi.org/10.1002/chin.201127237.

[39] L. Zeng, Z. Cheng, J. Fan, L.S. Fan, J. Gong, Metal oxide redox chemistry for chemical looping processes, Nat. Rev. Chem. 2 (2018) 1, https://doi.org/10.1038/s41570-018-0046-2.

[40] A. Löfberg, J. Guerrero-Caballero, T. Kane, A. Rubbens, L. Jalowiecki-Duhamel, $Ni/CeO_2$ based catalysts as oxygen vectors for the chemical looping dry reforming of methane for syngas production, Appl. Catal. B Environ. 212 (2017) 159–174, https://doi.org/10.1016/j.apcatb.2017.04.048.

[41] P.O. Schmidt, T. Rosenband, C. Langer, W.M. Itano, J.C. Bergquist, D.J. Wineland, Spectroscopy using quantum logic, Science 309 (2005) 749–752, https://doi.org/10.1126/science.1114375.

[42] D. Maiti, Y.A. Daza, M.M. Yung, J.N. Kuhn, V.R. Bhethanabotla, Oxygen vacancy formation characteristics in the bulk and across different surface terminations of $La_{(1-x)}\,Sr_x\,Fe_{(1-y)}\,Co_y\,O_{(3-\delta)}$ perovskite oxides for $CO_2$ conversion, J. Mater. Chem. A 4 (2016) 5137–5148, https://doi.org/10.1039/C5TA10284G.

[43] X. Yan, C. Duan, S. Yu, B. Dai, C. Sun, H. Chu, Revealing the mechanism of oxygen vacancy defect for $CO_2$ adsorption and diffusion on CaO: DFT and experimental study, J. $CO_2$ Util. 79 (2024) 102648, https://doi.org/10.1016/j.jcou.2023.102648.

[44] Y. Guo, C. Tan, P. Wang, J. Sun, W. Li, C. Zhao, P. Lu, Magnesium-based basic mixtures derived from earth-abundant natural minerals for $CO_2$ capture in simulated flue gas, Fuel 243 (2019) 298–305, https://doi.org/10.1016/j.fuel.2019.01.108.

[45] Z. Yuyuan, G. Zhiwei, S. Haocheng, W. Liang, Z. Shuang, L. Xipeng, C. Qicheng, C. Haisheng, The role of oxygen vacancy in $CaO-Ca_{12}Al_{14}O_{33}$ materials derived from hydrocalumite for enhanced $CO_2$ capture cyclic performance, Chem. Eng. J. 481 (2024) 147955, https://doi.org/10.1016/j.cej.2023.147955.

[46] C. Yang, J. Zhang, J. Wang, D. Li, K. Li, X. Zhu, Oxygen vacancies enriched $Ni-Co/SiO_2@CeO_2$ redox catalyst for cycling methane partial oxidation and $CO_2$ splitting, Chin. J. Chem. Eng. 63 (2023) 235–245, https://doi.org/10.1016/j.cjche.2023.04.025.

[47] A. Shokrollahi, S. Sharifnia, T. Hamoule, Probing $CO_2$ methanation enhancement on dendritic mesoporous silica nanoparticle supported alkaline-earth ion doped $LaNiO_3$-derived catalysts: the dominant role of $Ni^0$ active sites over oxygen vacancies, J. Environ. Chem. Eng. 12 (2024) 112606, https://doi.org/10.1016/j.jece.2024.112606.

[48] S. Molina-Ramírez, M. Cortés-Reyes, C. Herrera, M.A. Larrubia, L.J. Alemany, $CO_2$-SR Cyclic technology: $CO_2$ storage and *in situ* regeneration with $CH_4$ over a new dual function NiBa unsupported catalyst, J. $CO_2$ Util. 40 (2020) 101201, https://doi.org/10.1016/j.jcou.2020.101201.

[49] S. Molina-Ramírez, D. Peltzer, M. Cortés-Reyes, C. Herrera, M.A. Larrubia, L. Cornaglia, L.J. Alemany, $CO_2$-SR technology using NiBa unsupported catalyst. Isotopic study of cyclic process of $CO_2$ storage and *in situ* regeneration with $CH_4$, Fuel 341 (2023) 127690, https://doi.org/10.1016/j.fuel.2023.127690.

[50] M. Bououdina, D. Grant, G. Walker, Effect of processing conditions on unsupported Ni-based catalysts for graphitic-nanofibre formation, Carbon 43 (2005) 1286–1292, https://doi.org/10.1016/j.carbon.2004.12.026.

[51] S. Chen, M. Leng, Z. Liao, J. Zeng, H. Xie, G. Zhou, Synergistic effects of surface acidity and alkalinity of $Ni/\gamma-Al_2O_3$ catalysts in fats and oils hydrodeoxygenation product distribution, Ind. Crops Prod. 211 (2024) 118227, https://doi.org/10.1016/j.indcrop.2024.118227.

[52] G. George, S. Anandhan, Synthesis and characterisation of nickel oxide nanofibre webs with alcohol sensing characteristics, RSC Adv. 4 (2014) 62009–62020, https://doi.org/10.1039/C4RA11083H.

[53] N. Mironova-Ulmane, A. Kuzmin, I. Steins, J. Grabis, I. Sildos, M. Pärs, Raman scattering in nanosized nickel oxide NiO, J. Phys. Conf. Ser. 93 (2007) 012039, https://doi.org/10.1088/1742-6596/93/1/012039.

[54] R.E. Benner, J.R. Mitchell, R.W. Grow, Raman scattering as a diagnostic technique for cathode characterization, IEEE Trans. Electron Devices 34 (1987) 1842–1847, https://doi.org/10.1109/T-ED.1987.23163.

[55] J.T.H. Kwan, A. Bonakdarpour, G. Afonso, D.P. Wilkinson, Bridging fundamental electrochemistry with applied fuel cell testing: a novel and economical rotating disk electrode tip for electrochemical assessment of catalyst-coated membranes, Electrochim. Acta 258 (2017) 208–219, https://doi.org/10.1016/j.electacta.2017.10.087.

[56] O. Karslıoğlu, L. Trotochaud, I. Zegkinoglou, H. Bluhm, X-ray spectroscopic characterization of BaO, $Ba(OH)_2$, $BaCO_3$, and $Ba(NO_3)_2$, J. Electron Spectrosc. Relat. Phenom. 225 (2018) 55–61, https://doi.org/10.1016/j.elspec.2018.03.008.

[57] J.F. Moulder, W.F. Stickle, D.B. Kenneth, P.E. Sobol, Handbook of X-Ray Photoelectron Spectroscopy, Perkin-Elmer Corporation, Physical Electronics Inc, USA, 1992.
[58] M. Cortés-Reyes, Coupling of After-Treatment Technologies for Zero Emissions in Light Vehicles, Universidad de Málaga, 2016.
[59] A. Martínez-Arias, M. Fernández-García, V. Ballesteros, L.N. Salamanca, J. C. Conesa, C. Otero, J. Soria, Characterization of high surface area Zr−Ce (1:1) mixed oxide prepared by a microemulsion method, Langmuir 15 (1999) 4796–4802, https://doi.org/10.1021/la981537h.
[60] E. Zacharaki, P. Beato, R.R. Tiruvalam, K.J. Andersson, H. Fjellvåg, A.O. Sjåstad, From colloidal monodisperse nickel nanoparticles to well-defined $Ni/Al_2O_3$ model catalysts, Langmuir 33 (2017) 9836–9843, https://doi.org/10.1021/acs.langmuir.7b02197.
[61] C. Liang, L. Zhang, Y. Zheng, S. Zhang, Q. Liu, G. Gao, D. Dong, Y. Wang, L. Xu, X. Hu, Methanation of $CO_2$ over nickel catalysts: impacts of acidic/basic sites on formation of the reaction intermediates, Fuel 262 (2020) 116521, https://doi.org/10.1016/j.fuel.2019.116521.
[62] M. Usman, S. Podila, A.A. Al-Zahrani, Role of perovskites phase in Ni-based catalysts for low temperature $CO_2$ methanation, Int. J. Hydrog. Energy 95 (2024) 173–184, https://doi.org/10.1016/j.ijhydene.2024.11.255.
[63] L. Nie, Y. Mu, J. Jin, J. Chen, J. Mi, Recent developments and consideration issues in solid adsorbents for $CO_2$ capture from flue gas, Chin. J. Chem. Eng. 26 (2018) 2303–2317, https://doi.org/10.1016/j.cjche.2018.07.012.
[64] C.F. Imbachi-Gamba, C. Toncón, K. Sapag, L. Cornaglia, J. Múnera, Novel organic acid treatment to enhance the performance of MgO-based sorbents in the $CO_2$ capture at intermediate temperatures, J. Environ. Chem. Eng. 13 (2025) 116240, https://doi.org/10.1016/j.jece.2025.116240.
[65] A. Nawar, M. Ali, A.H. Khoja, A. Waqas, M. Anwar, M. Mahmood, Enhanced $CO_2$ capture using organic acid structure modified waste eggshell derived CaO sorbent, J. Environ. Chem. Eng. 9 (2021) 104871, https://doi.org/10.1016/j.jece.2020.104871.
[66] J. Hu, P. Hongmanorom, J. Chen, W. Wei, P. Chirawatkul, V.V. Galvita, S. Kawi, Tandem distributing Ni into CaO framework for isothermal integration of $CO_2$ capture and conversion, Chem. Eng. J. 452 (2023) 139460, https://doi.org/10.1016/j.cej.2022.139460.
[67] P. Zhang, J. Tong, K. Huang, Combining electrochemical $CO_2$ capture with catalytic dry methane reforming in a single reactor for low-cost syngas production, ACS Sustain. Chem. Eng. 4 (2016) 7056–7065, https://doi.org/10.1021/acssuschemeng.6b01960.